International Journal of Plasticity 160 (2023) 103510

Contents lists available at ScienceDirect

International Journal of Plasticity

journal homepage: www.elsevier.com/locate/ijplas

Room-temperature plastic deformation of single crystals of α-manganese - hard and brittle metallic element

Kyosuke Kishida [a,b,*], Hirotaka Suzuki [a], Masaomi Okutani [a], Haruyuki Inui [a,b]

[a] Department of Materials Science and Engineering, Kyoto University, Sakyo-ku, Kyoto 606-8501, Japan
[b] Center for Elements Strategy Initiative for Structural Materials (ESISM), Kyoto University, Sakyo-ku, Kyoto 606-8501, Japan

ARTICLE INFO

Keywords:
Manganese
Deformation structure
Dislocations
Mechanical properties
Micropillar compression

ABSTRACT

The deformation behavior of single crystals of α-manganese has been investigated by micropillar compression at room temperature as a function of crystal orientation and specimen size. When the specimen size is reduced to the micrometer-range, single crystals of α-manganese are found to plastically deform by dislocation motion at room temperature for the first time, accompanied by very high yield stresses of the range of 4–6 GPa. Slip along [111] and [001] are identified to operate for compression axis orientations near [001] and near [011] and [$\bar{1}$11], respectively. Any low-indexed planes cannot be designated as the slip plane for both slip along [111] and [001], because of the significantly wavy nature of slip lines caused by the occurrence of frequent cross-slip. Slip along [111] tends to prefer the slip plane of {112} rather than {110}. Slip along [001], on the other hand, tends to occur on the maximum resolved shear stress plane. The 1/2[111] dislocation carrying slip along [111] moves as a perfect dislocation without dissociating into partials and does not have any preferred orientation. The [001] dislocation carrying slip along [001] also moves as a perfect dislocation without dissociating into partials. Although the Peierls stress for the motion of these dislocations must be very high, there seems no deep Peierls valleys along particular directions, unlike the screw direction for the 1/2[111] dislocation in body-centered cubic metals.

1. Introduction

Manganese is ubiquitous and familiar in many research laboratories and is used heavily in industries in the forms of alloys and compounds. The vast majority of the total demand of manganese is in steel making because of its ability of sulfur-fixing, deoxidizing, increasing strength and improving high-temperature workability (ASM Int. Handbook Comm., 1990; Matricardi and Downing, 2000; Sully, 1955). Manganese is also very important as an alloying element to nonferrous metals such as aluminum alloys used for beverage cans, in which approximately 1.5 wt.% manganese is added to increase resistance to corrosion and strength of aluminum (Kaufman, 2000; Matricardi and Downing, 2000; Sully, 1955). In addition, manganese dioxide has been used as the cathode material for commercial disposable dry batteries of both the standard (zinc-carbon) and alkaline types, and lithium manganese phosphate ($LiMnPO_4$) is considered for the use as a cathode material of lithium-ion batteries in the future (Dell, 2000; Martha et al., 2009).

Manganese is known to undergo isotropic phase transformations upon cooling, starting from δ to γ (at 1134 °C), then to β (at 1095 °C), and finally to α (at 742 °C) (Meaden, 1968; Sully, 1955). While the δ and γ phases respectively possess simple b.c.c.

* Corresponding author.
E-mail address: kishida.kyosuke.6w@kyoto-u.ac.jp (K. Kishida).

https://doi.org/10.1016/j.ijplas.2022.103510
Received 31 October 2022; Received in revised form 18 December 2022;
Available online 30 December 2022

(body-centered cubic) and f.c.c. (face-centered cubic) structures, the β and α phases are known to possess complicated crystal structures containing 20 and 58 atoms in the cubic unit cell, respectively. In particular, α-manganese is often described as a typical example of metallic elements with very complex crystal structures. α-manganese possesses a complex crystal structure of the A12 type (in the Strukturbericht symbol) based on the body-centered cubic lattice with the lattice parameter $a \sim 8.9$ Å, the space group of $I\bar{4}3$ m (No. 217) and the Pearson symbol of *cI*58 (Proult and Donnadieu, 1995). This crystal structure is usually described as one of those formed with the packing of coordination polyhedra, as many other complicated crystal structures are (Proult and Donnadieu, 1995; Watson and Bennett, 1985). The A12 structure of α-manganese is also considered to be made up of four different kinds of corrugated atomic layers designated as *A, A*', *B* and *B*' stacked along the ⟨001⟩ cube axis with the stacking sequence of *AB*'*BA*' (Fig. 1(a)) (Frank and Kasper, 1959). These four layers of *A* (between $z = 0$ and $z = 1/4$), *B*'(between $z = 1/4$ and $z = 1/2$), *B* (between $z = 1/2$ and $z = 3/4$) and *A*' (between $z = 3/4$ and $z = 1$) have an identical atomic arrangement of the corrugated hexagonal-type, in which layers *A* and *A*' share the atom at the corner of the unit cell and layers *B* and *B*' share the body-center atom (the shared atoms are indicated with yellow in Fig.1). The corrugated atomic layers of *A* and *A*' as well as those of *B* and *B*' are related to each other by the $\bar{4}$ rotoinversion operation, whose inversion axis is parallel to ⟨001⟩ with the inversion centers at (0,0,0) or (1/2,1/2,1/2). Layers *A* and *B* as well as those of *A*' and *B*' are simply correlated with each other by the translation operation of $\boldsymbol{t} = \mathbf{a}/2 + \boldsymbol{b}/2 + \boldsymbol{c}/2$. Since manganese is rarely used as a pure element, nothing is known not only about its workability such as formability and drawability but also about plastic deformation mechanisms such as operative slip systems and their critical resolved shear stresses (CRSSs) to the best of the authors' knowledge. In most cases, manganese is simply stated to be 'hard and brittle', but it is not clear at all how and why manganese is hard and brittle (Matricardi and Downing, 2000; Sully, 1955). Microcracks introduced during phase transformations upon solidification are sometimes pointed out to be one of the main causes for the brittleness, as transformation strains are accumulated during multiple phase transformations. While this is likely the case, some questions still remain, such as whether plastic flow can occur by dislocation motion in the absence of these microcracks in manganese, and if so, what the Burgers vector of these dislocations is, and on what plane these dislocations can slip, and so on.

Recently, micropillar compression testing has gradually been recognized to be capable not only of elucidating the specimen-size dependent deformation behaviors of ductile materials (Cui et al., 2020; Dehm et al., 2018; Dunstan and Bushby, 2013; Kratochvíl et al., 2016; Lin et al., 2016; Mapar et al., 2017; Uchic et al., 2009; Weaver et al., 2018; Zhang et al., 2013, 2017; Zhao et al., 2019) but also of studying the ambient-temperature deformation behaviors of hard and brittle materials (Csanádi et al., 2019; Korte and Clegg, 2011; Korte-Kerzel, 2017; Michler et al., 2007; Schröders et al., 2018; Takata et al., 2013). We have successfully applied this technique to study ambient-temperature deformation behaviors of some brittle materials such as SiC, transition-metal (TM) diborides, TM

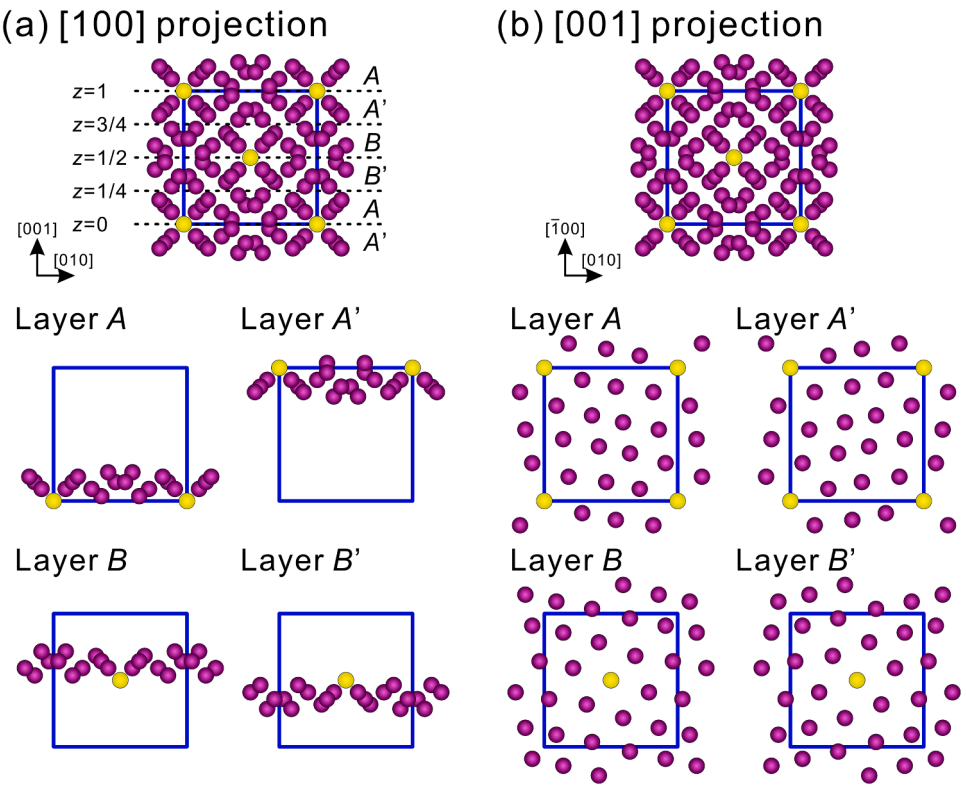

Fig. 1. (a) [100] and (b) [001] projections of the crystal structure of α-manganese, which is made up of four different kinds of corrugated atomic layers designated as *A, A*', *B* and *B*' stacked along the ⟨001⟩ cube axis with the stacking sequence of *AB*'*BA*'. The atomic arrangements in each of the corrugated atomic layers of *A, A*', *B, B*' are indicated below. Because of the cubic symmetry, these cubic axes can be interchanged.

silicides of the $TMSi_2$ type and of the TM_5Si_3-type, Ti_3SiC_2, a series of Fe-Zn intermetallics in the coating layer of galvannealed steel, FeCr (sigma-phase) and so on, deducing the operative slip systems and their CRSS values (Chen et al., 2021; Hashizume et al., 2020, 2021; Higashi et al., 2018; Inui et al., 2018; Kishida et al., 2018, 2020a, 2020b, 2020c, 2020d, 2022a, 2022b, 2022c; Okamoto et al., 2013, 2014)). Plastic flow observed at ambient temperature for these hard and brittle materials is obviously due largely to the small specimen size reduced down to the micrometer order in micropillar compression, but this is not always the case as only brittle failure without any appreciable plastic flow is observed for some brittle materials such as Mo_5Si_3 (Kishida et al., 2022a) and Γ_1-FeZn intermetallic (Okamoto et al., 2013). This indicates that micropillar compression testing may offer a high chance to observe plastic flow at ambient temperature for α-manganese, thereby, to deduce the deformation mechanisms (operative slip systems and their CRSS values).

In the present study, we investigate the plastic deformation behavior of single crystals of α-manganese in compression as a function of crystal orientation at room temperature with the use of micropillar specimens of a size range of 1.0∼10.5 μm, in order to deduce the ambient-temperature deformation mechanism through identifying all the operative slip systems and evaluating their CRSS values.

2. Experimental procedure

Electrolytically refined manganese chips of the purity grade 5 N, obtained from Osaka Asahi Co., Ltd., were used to prepare specimens for micropillar compression testing. After mechanical polishing with diamond past to mirror finish, single-crystal micropillar specimens with square cross-sections having aspect ratios of ∼3:1 (height to edge length) were machined from the chips with a JEOL JIB-4000 focused-ion beam (FIB) apparatus at an operating voltage of 30 kV. The edge lengths (L) of the square cross-sections (hereafter referred to as "specimen size" throughout the paper) ranged from 1.0 to 10.5 μm. A square cross-section was employed to facilitate the identification of slip planes and slip directions. The compression-axis orientations of these micropillar specimens as well as their side-face orientations were examined by electron backscatter diffraction (EBSD) in a JEOL JSM-7001FA field-emission scanning electron microscope (FE-SEM). Nine different compression-axis orientations A∼I were selected (Fig. 2) because slip along either ⟨111⟩ or ⟨001⟩ were found to occur on wavy slip planes, and therefore the investigation of the loading axis dependence of slip planes was considered to be essential as described later in Section 3.2. The Schmid factors for some possible slip systems for each of the nine orientations are tabulated in Table 1 on the assumption that the low indexed lattice planes {100}, {110} and {112} together with the maximum resolved shear stressed plane (MRSSP) are possible slip planes for crystals with the body-centered cubic lattice. As seen in Table 1, ⟨111⟩ slip is favored for orientations A∼D and G∼I, while ⟨001⟩ slip is favored for orientations E∼I when judged from their Schmid factors (> 0.46). The loading axis dependence of the Schmid factors for [111] and [001] slip on the low-indexed lattice planes and the MRSSP are summarized in the supplementary figure (Fig. S1).

Compression tests were conducted for micropillar specimens with a flat punch indenter tip on an Agilent Technologies Nano Indenter G200 nanomechanical tester at room temperature under the displacement-rate-controlled mode at a nominal strain rate of $1 \times 10^{-4}\ s^{-1}$. Slip planes were determined by slip trace analysis made on two orthogonal surfaces of the deformed micropillar specimen by scanning electron microscopy (SEM) with a JEOL JSM-7001FA electron microscope. Deformation microstructures developed in the deformed micropillars were investigated by transmission electron microscopy (TEM) and scanning transmission electron microscopy (STEM) with JEOL JEM-2100F and JEM-ARM200F. Specimens for TEM/STEM observations were prepared by FIB-SEM in-situ lift-out technique using a FEI Quanta 3D 200i Dual-Beam system equipped with an Omniprobe nanomanipulator.

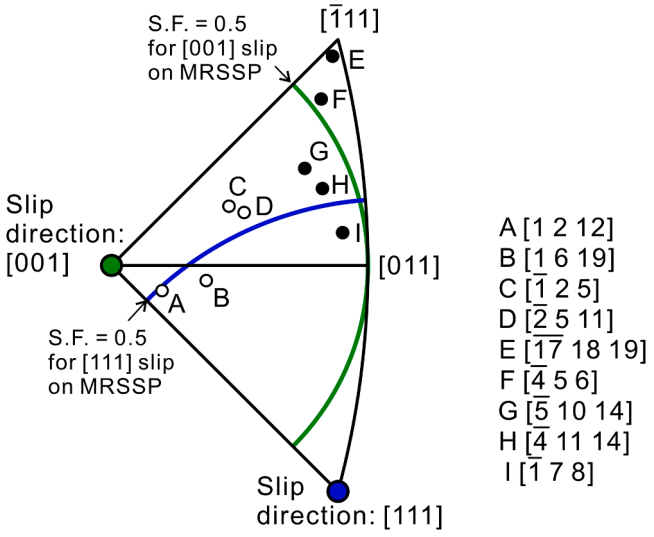

Fig. 2. Stereographic projection of the loading-axis orientations selected.

Table 1
The Schmid factor values for some possible slip systems in α-manganese single crystals with the nine different loading-axis orientations A~I. For {112}[111] slip and {110}[001] slip, the highest Schmid factor values are indicated.

Slip direction	[111]			[001]		
b (Å)	7.71			8.91		
Slip plane	$(\bar{1}01)$	{112}	MRSSP	$\{\bar{1}10\}$	(010)	MRSSP
A [1 2 12]	0.452	0.498	0.500	0.171	0.161	0.180
B [1 6 19]	0.480	0.477	0.496	0.236	0.286	0.290
C $[\bar{1}\ 2\ 5]$	0.489	0.424	0.490	0.354	0.333	0.373
D $[\bar{2}\ 5\ 11]$	0.495	0.440	0.496	0.363	0.367	0.395
E $[\bar{1}\bar{7}\ 18\ 19]$	0.301	0.344	0.344	0.483	0.351	0.483
F $[\bar{4}\ 5\ 6]$	0.371	0.407	0.409	0.496	0.390	0.499
G $[\bar{5}\ 10\ 14]$	0.459	0.474	0.484	0.463	0.436	0.488
H $[\bar{4}\ 11\ 14]$	0.463	0.491	0.497	0.446	0.462	0.492
I $[\bar{1}\ 7\ 8]$	0.451	0.492	0.495	0.397	0.491	0.496

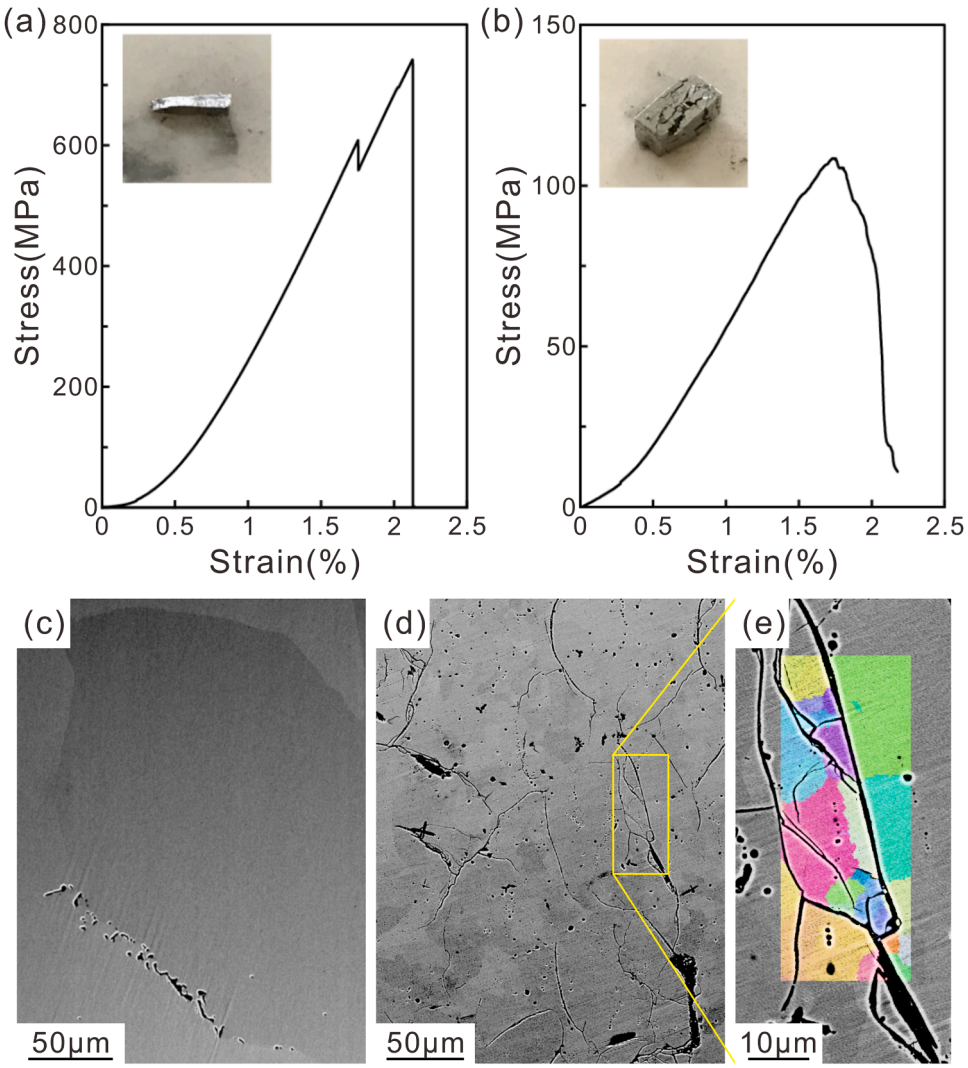

Fig. 3. Typical compression stress-strain curves of bulk polycrystals of α-manganese prepared by cutting (a) directly from the electrolytically refined chip and (b) from the ingot prepared by the arc-melting of the chips. The appearance of specimens after failure is also indicated in the inset of the figure. The specimen size was 1 × 1 × 3 mm^3 and compression tests were made at a strain rate of $10^{-4}\ s^{-1}$ at room temperature. (c-e) SEM backscattered electron images of these two bulk polycrystals before compression, (c) electrolytically refined chip and (d,e) arc-melted and heat-treated specimen. (e) magnified view of the marked area in (d) overlayed with EBSD orientation map, indicating many cracks are formed mainly along grain boundaries.

3. Results

3.1. Bulk deformation

When tested in compression, premature failure occurs without any appreciable plastic strain in bulk polycrystals (measuring 1 × 1 × 3 mm^3) of α-manganese (Figs. 3(a) and (b)). This is consistent with what is believed for the deformability of α-manganese for a long time. The fracture stress is higher for specimens cut directly from the electrolytically refined chips (~750 MPa) than for those cut from the ingots prepared by the arc-melting and subsequent heat-treatment at 650 °C for 5 h of the chips (~100 MPa). Figs. 3(c-e) show SEM backscattered electron images of these two bulk polycrystals before compression. Many cracks as well as many voids are observed mainly along grain boundaries in the arc-melted and heat-treated specimen (Figs. 3(d) and (e), grain size: 5~30 μm), while such defects are rarely seen in the electrolytically refined specimen with a relatively large grain size (100 μm ~ 1 mm) (Fig. 3(c)). These observations together with the observed difference in fracture stress clearly indicate that the existence of cracks and voids introduced during phase transformations is one of the main causes for the extreme brittleness of α-manganese polycrystals. However, the fact that both specimens failed by vertical cracking in compression (Figs. 3(a) and (b) implies also the intrinsic brittleness of α-manganese.

3.2. Stress-strain behavior and slip trace observation

Figs. 4(a) and (b) show selected stress-strain curves obtained for micropillar specimens with the A-D and E~I orientations, respectively. Compression tests were interrupted at plastic strain of about 0.5 ~1% in most cases before failure occurs (> 1~2% plastic strain) for the ease of slip line observations. Surprisingly, plastic flow occurs even at room temperature in α-manganese for all crystal orientations tested. In most cases, elastic-plastic transition occurs very smoothly without showing any strain burst behavior that is generally observed as a flat portion in the stress-strain curve. The yield stress is thus defined as the 0.2% proof stress, as indicated by arrows in Figs. 4(a) and (b). The yield stresses are very high in the range of 4–6 GPa for all orientations, but any strong specimen-size dependence of yield stress is not observed for all the orientations investigated. It is thus evident that α-manganese single crystals are fairly deformable in compression at room temperature when the specimen size is reduced to the micrometer order, unlike the bulk polycrystals (Fig. 3).

Figs. 5(a)-(d) show SEM secondary electron images of deformation structures observed on two orthogonal surfaces of micropillar specimens with the A~D orientations, respectively. The observations were made along the direction inclined by 30° from the loading axis. A square cross-section was employed to facilitate the identification of slip planes and slip directions. The possible slip direction for these orientations is [111] (Table 1) and the [111] direction was set to lie on one of the two orthogonal side faces for the ease of to

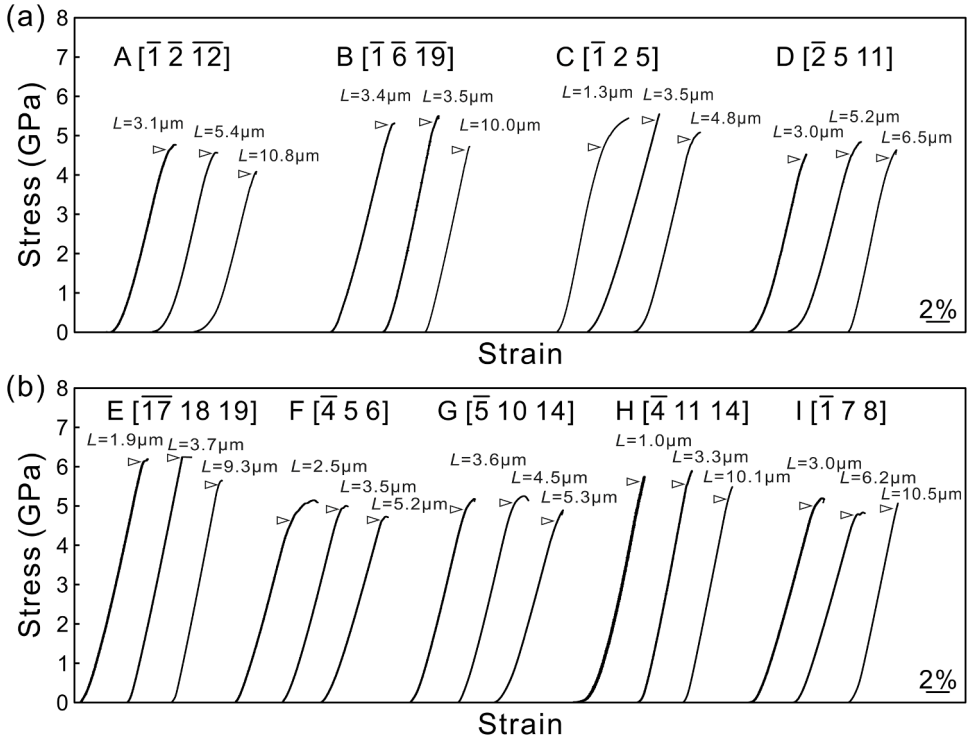

Fig. 4. Selected stress-strain curves obtained in compression for micropillar specimens with (a) A~D and (b) E~I orientations, respectively. The specimen sizes are indicated in the figures and arrows indicate the yield points deduced as the 0.2% proof stress.

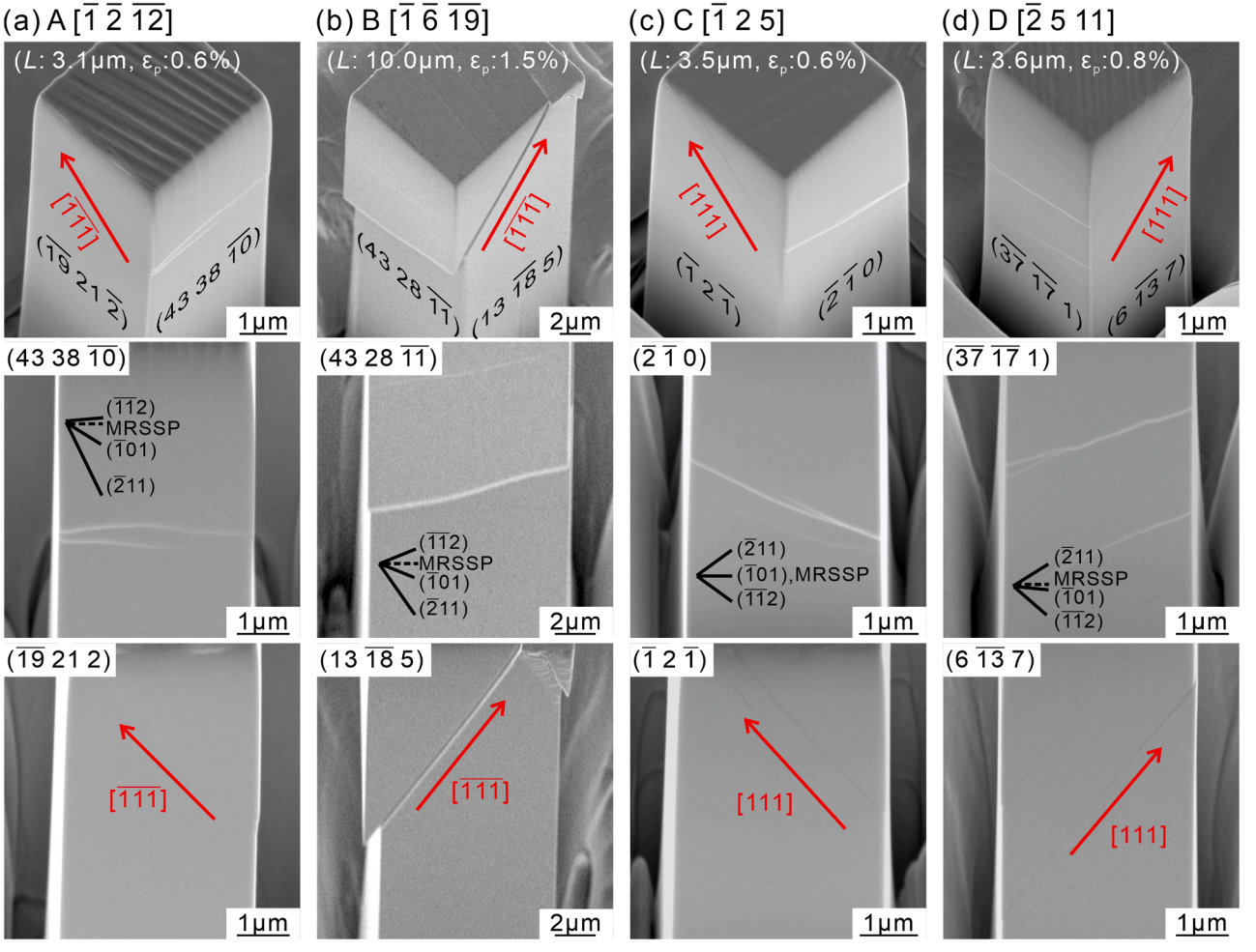

Fig. 5. Deformation markings observed on two orthogonal surfaces of α-manganese single- crystal micropillar specimens with (a) A ([$\bar{1}$ $\bar{2}$ $\bar{1}\bar{2}$]), (b) B ([$\bar{1}$ $\bar{6}$ $\bar{1}\bar{9}$]), (c) C ([$\bar{1}$25]) and (d) D ([$\bar{2}$ 5 11]) orientations. Two orthogonal side surfaces of the top row are presented in the middle and bottom rows for each of orientations. Images in the middle and bottom rows are vertically enlarged 200% from the original images so as to make the trace analysis easier. Traces of possible slip planes of low-indices are indicated in the middle row.

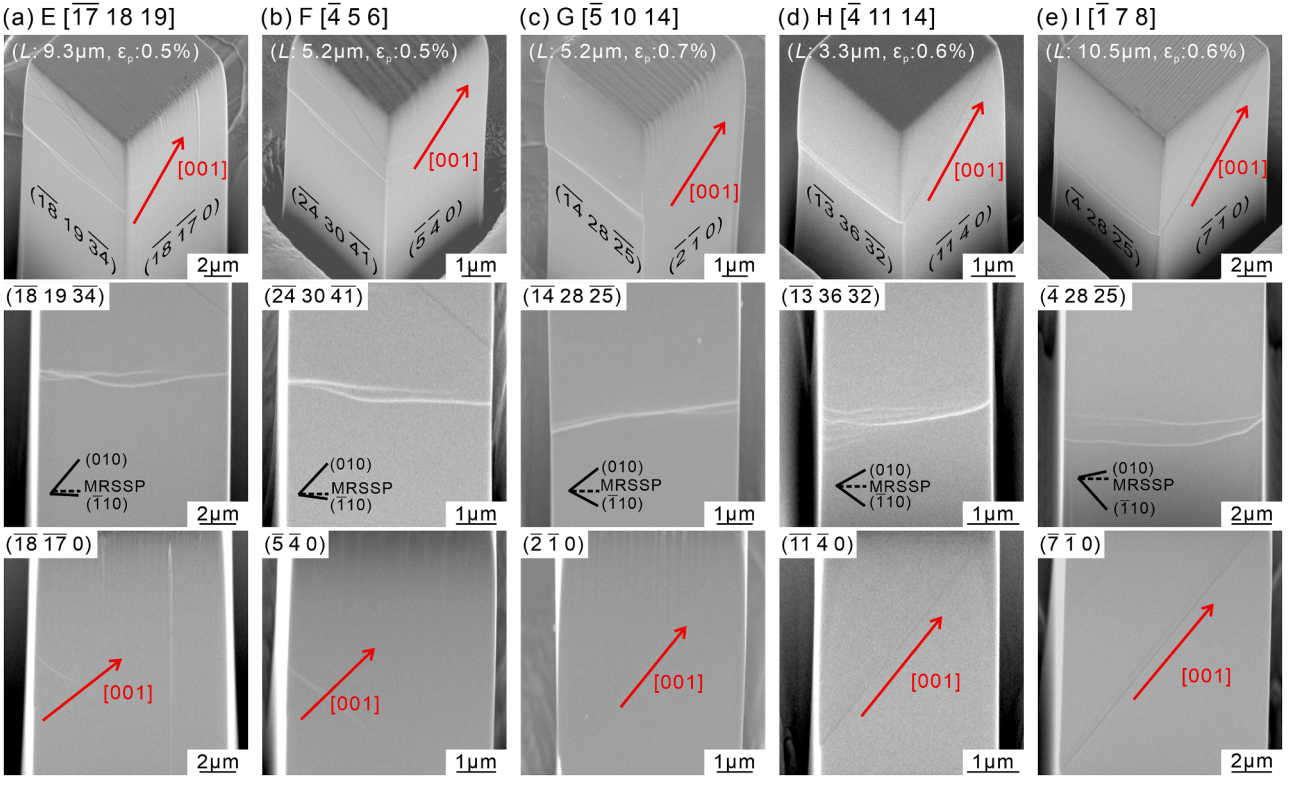

Fig. 6. Deformation markings observed on two orthogonal surfaces of α-manganese single- crystal micropillar specimens with (a) E ([$\bar{1}\bar{7}$ 18 19]), (b) F [$\bar{4}$ 5 6], (c) G ([$\bar{5}$ 10 14]), (d) H ([$\bar{4}$ 11 14]) and (e) I ([$\bar{1}$ 7 8]) orientations. Two orthogonal side surfaces of the top row are presented in the middle and bottom rows for each of orientations. Images in the middle and bottom rows are vertically enlarged 200% from the original images so as to make the trace analysis easier. Traces of possible slip planes of low-index are indicated in the middle row.

facilitate the identification of slip planes and slip directions. For all of the loading orientations, faint but very straight slip lines are observed on the side face on which the [111] direction was set to lie ($(\bar{1}9\ 21\ \bar{2})$, $(13\ \bar{1}8\ 5)$, $(\bar{1}2\bar{1})$ and $(6\bar{1}\bar{3}7)$ side faces for orientations A~D, respectively; the bottom row of Fig. 5), confirming the [111] slip direction. However, slip lines observed on another side face (the middle row of Fig. 5) were considerably wavy and it is practically impossible to determine the slip plane uniquely by trace analysis. The results of trace analysis made for micropillar specimens with the A~D orientations are plotted in Fig. 7(a) as a ψ-χ plot, following the conventional method employed for body-centered cubic (BCC) metals (Christian, 1983; Weinberger et al., 2013) where ψ is the angle between the $(\bar{1}01)$ plane and observed slip plane and χ is the angle between the $(\bar{1}01)$ plane and maximum resolved shear stress plane (MRSSP). In Fig. 7, the angular ranges, each defined by the maximum and minimum ψ values observed for each loading axis orientation are plotted. Fig. 7(a) clearly indicates that the slip along the [111] direction does occur neither on a particular slip plane of low-index such as $(\bar{1}\bar{1}2)$, $(\bar{1}01)$ and $(\bar{2}11)$ nor on the MRSSP, although either {110} or {112} can be considered to be a fundamental slip plane. While it is very difficult to find out BCC metals with a similar ψ-χ relation, Fig. 7(a) may indicate the preference of {112} slip rather than {110} slip in α-manganese when the slip occurs along the [111] direction.

Figs. 6(a)-(e) show SEM secondary electron images of deformation structures observed on two orthogonal surfaces of micropillar specimens with the E~I orientations, respectively. The observations were made similarly along the direction inclined by 30° from the loading axis and a square cross-section was employed to facilitate the identification of slip planes and slip directions. The possible slip direction for these orientations is [001] (Table 1) and the [001] direction was set to lie on one of the two orthogonal side faces for the ease of to facilitate the identification of slip planes and slip directions. Similarly to orientations A~D, faint but very straight slip lines are observed on the side face on which the [001] direction was set to lie $((\bar{1}8\bar{1}70)$, $(\bar{5}40)$, $(\bar{2}\bar{1}0)$, $(\bar{1}\bar{1}40)$ and $(\bar{7}\bar{1}0)$ side faces for orientations E~I, respectively; the bottom row of Fig. 6), confirming the [001] slip direction. However, slip lines observed on another side face (the middle row of Fig. 6) were considerably wavy, making it practically impossible to determine the slip plane uniquely by

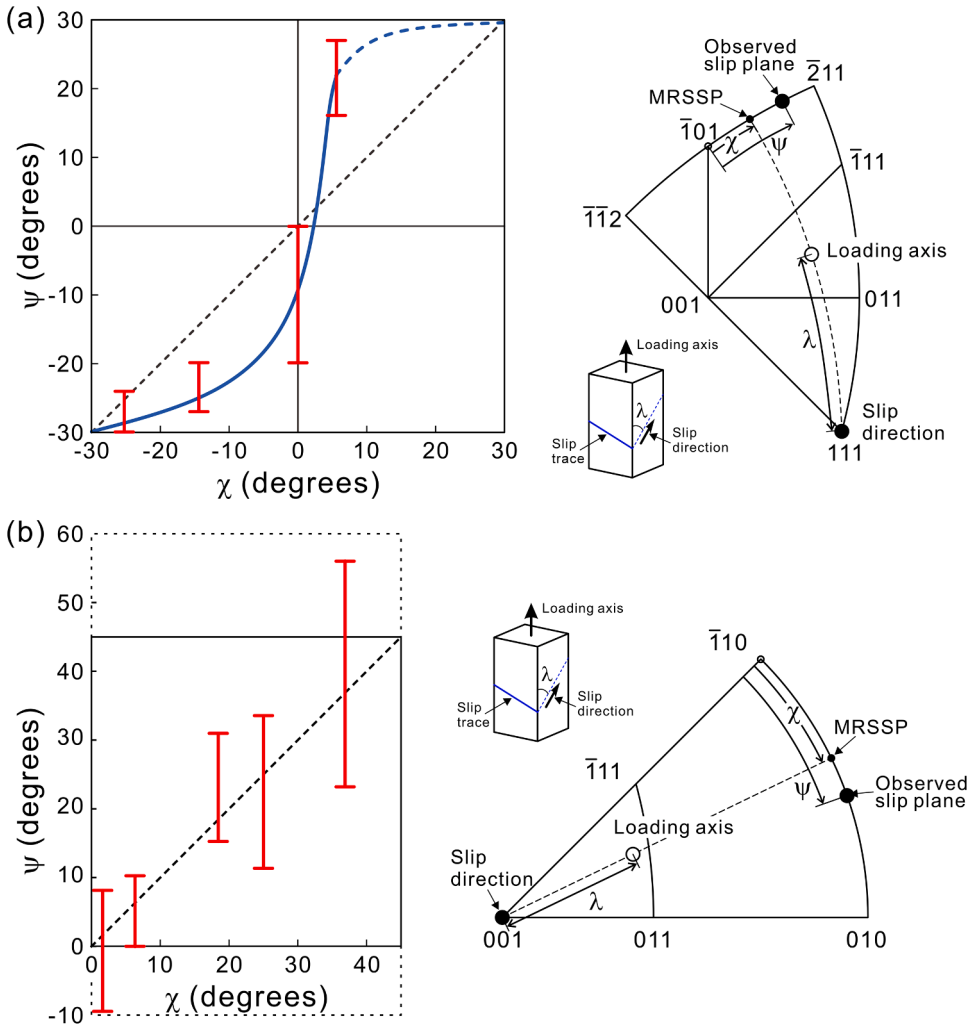

Fig. 7. ψ-χ relationships of slip along (a) [111] and (b) [001].

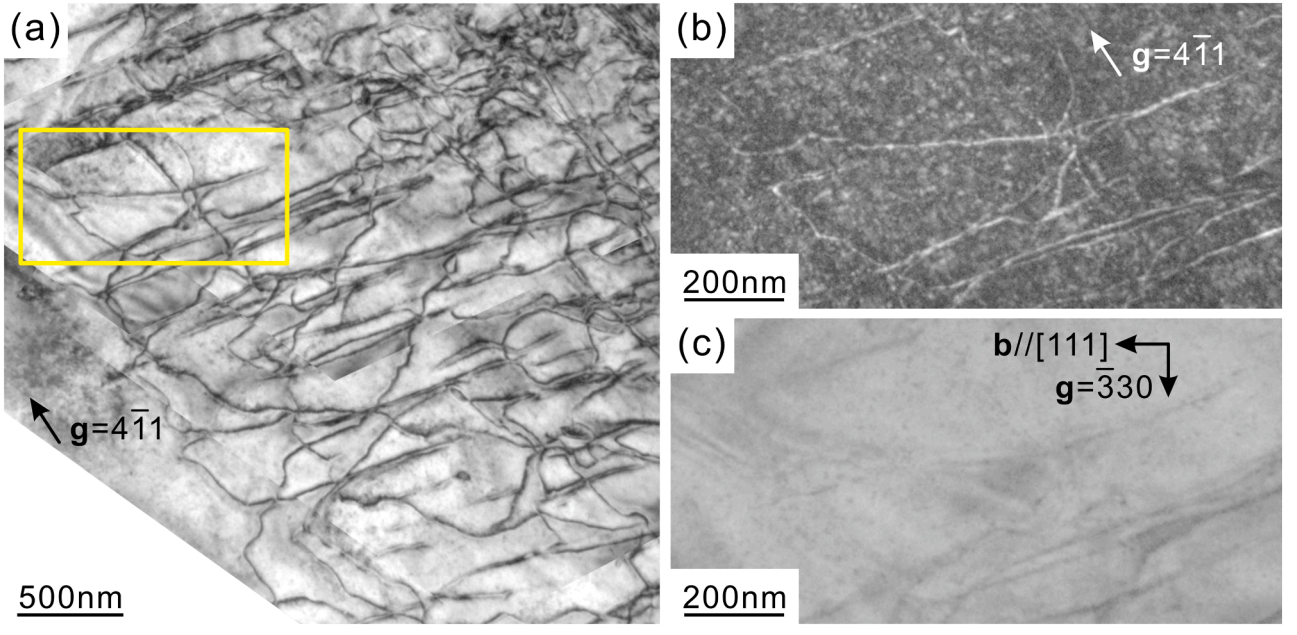

Fig. 8. TEM dislocation structures observed in a specimen with the orientation A ([$\bar{1}$ $\bar{2}$ $\bar{1}\bar{2}$]). (a) Bright-field image obtained with $\boldsymbol{g} = 4\bar{1}1$, (b) weak-beam dark-field image ($\boldsymbol{g} = 4\bar{1}1$) and (c) bright-filed image ($\boldsymbol{g} = \bar{3}30$) of the marked area in (a).

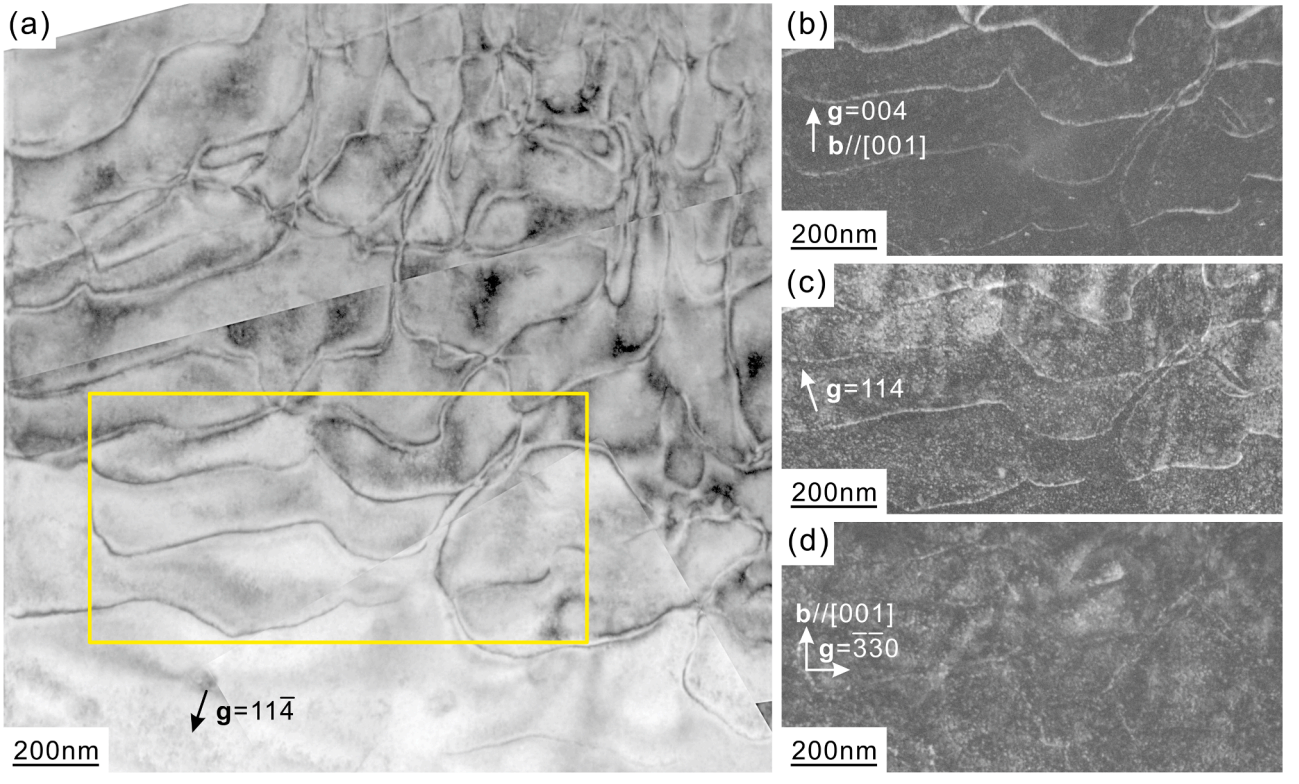

Fig. 9. TEM dislocation structures observed in a specimen with the orientation F ([$\bar{4}$ 5 6]). (a) Bright-field image obtained with $\boldsymbol{g} = 11\bar{4}$, and (b-d) weak-beam dark-field images of the marked area in (a) obtained with (b) $\boldsymbol{g} = 004$, (c) $\boldsymbol{g} = 114$ and (d) $\boldsymbol{g} = \bar{3}\bar{3}0$.

trace analysis. The results of trace analysis made for micropillar specimens with the E~I orientations are plotted in Fig. 7(b) as a ψ-χ plot, in which ψ is the angle between the $(\bar{1}10)$ plane and observed slip plane and χ is the angle between the $(\bar{1}10)$ plane and MRSSP. Fig. 7(b) clearly indicates that the slip along the [001] direction does not occur on a particular slip plane of low index such as (010) and $(\bar{1}10)$ (possible low-indexed planes) but tends to occur on the MRSSP.

3.3. Dislocation structure and dissociation

Dislocation structures observed in a specimen with orientation A ($[\bar{1}\,\bar{2}\,\bar{1}2]$) are shown in Figs. 8(a)-(c). The thin foil of Fig. 8 was cut parallel to the $(\bar{1}\bar{1}2)$ plane. Dislocations observed in Figs. 8(a) and (b) (imaged with the reflection vector (**g**) of $4\bar{1}1$) are invisible in Fig. 8(c) (imaged with $\boldsymbol{g}=\bar{3}30$). This indicates that the Burgers vector of these dislocations is $\boldsymbol{b} = 1/2[111]$, which is consistent with the result of slip trace analysis of Fig. 5. There seems no particular direction for these dislocations to align and no dislocation dissociation was noticed in the weak-beam image (Fig. 8(b)). The absence of dislocation dissociation is consistent with the occurrence of frequent cross-slip (Fig. 5).

Dislocation structures observed in a specimen with orientation F are shown in Figs. 9(a)-(d). The thin foil of Fig. 9 was cut parallel to the $(\bar{1}10)$ plane. Dislocations observed in Figs. 9(a), (b) and (c) (imaged with $\boldsymbol{g} = 11\bar{4}$, $\boldsymbol{g} = 004$ and $\boldsymbol{g} = 114$, respectively) are invisible in Fig. 9(d) (imaged with $\boldsymbol{g}=\bar{3}\bar{3}0$). This indicates that the Burgers vector of these dislocations is $\boldsymbol{b}$= [001], which is consistent with the result of slip trace analysis of Fig. 6. Many of these dislocations tend to align roughly parallel to their edge orientation, forming cusps on the slip plane. Dislocation dissociation into partials is not visible at least in the resolution limit of weak-beam microscopy (Fig. 9(b) and (c)). The absence of dislocation dissociation is consistent with the occurrence of frequent cross-slip (Fig. 6).

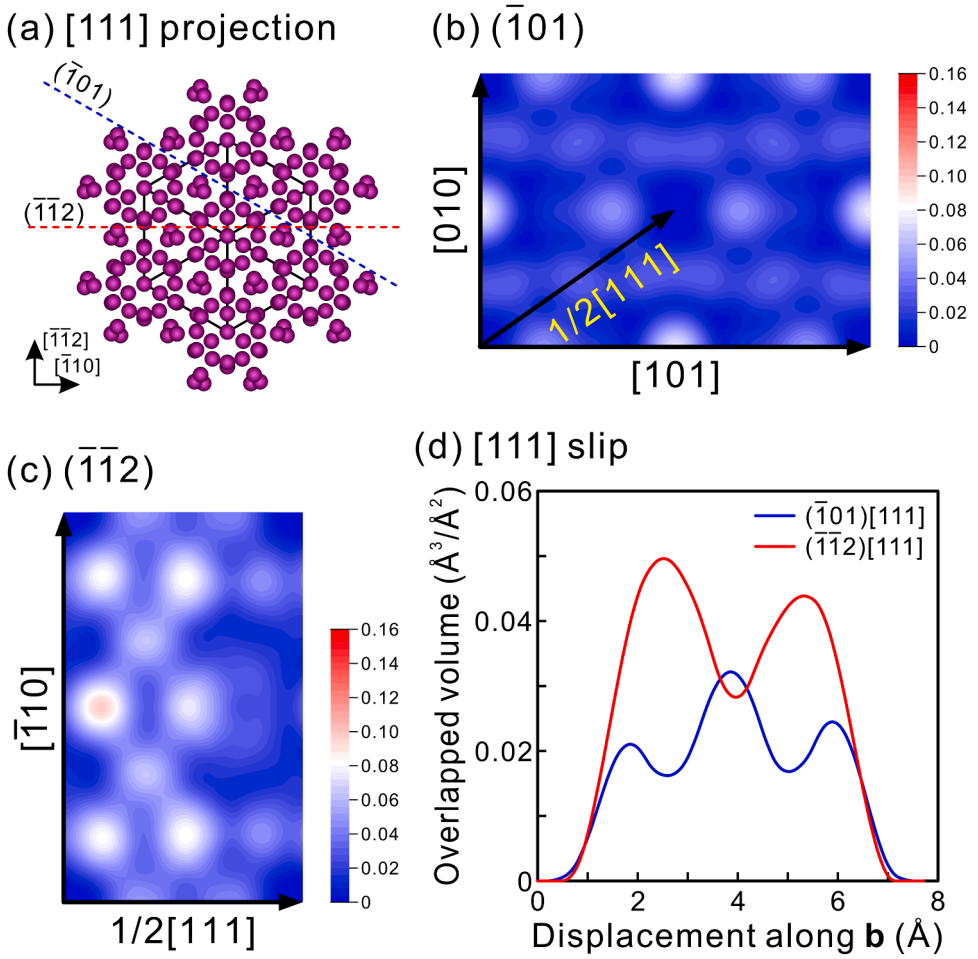

Fig. 10. (a) [111] projection of the crystal structure of α-manganese, showing the positions of $(\bar{1}01)$ and $(\bar{1}\bar{1}2)$ slip planes with the minimum overlapped volume for shear along [111] among the relevant non-equivalent planes. Two-dimensional views of overlapped atomic volumes on (b) $(\bar{1}01)$ and (c) $(\bar{1}\bar{1}2)$ slip planes indicated in (a). (d) Cross-sectional views of overlapped atomic volume along the slip direction of [111] on the $(\bar{1}01)$ and $(\bar{1}\bar{1}2)$ slip planes.

4. Discussion

4.1. Operative slip systems

While the slip directions are determined from trace analysis and TEM observations to be [111] and [001], there slip planes could not determined uniquely as a particular low-indexed plane because of the wavy nature of slip lines. In order to get insight into some plausible inherent slip planes for slip along [111] and [001], we calculate the overlapped atomic volume when shear occurs on a particular slip planes (such as {110} and {001}) (Figs. 10 and 11). Consider that a block of crystal is cut along a selected slip plane and the upper part of the block is displaced with respect to the lower part by a displacement vector **f** on the slip plane. Then, some atoms in the upper block overlap with those in the lower block and the total overlap atomic volume can be calculated as a function of **f** assuming all atoms are hard spheres with the atomic radius of 1.12 Å. A two-dimensional map of the overlap atomic volume can be created by repeating the procedure for various **f** covering the in-plane unit cell on the selected slip plane. The easier slip is expected for the displacement with smaller overlap volume as a first approximation. The minima in the two-dimensional overlapped atomic volume plot suggests the possible existence of stable stacking faults at the displacement, which can be used as a guide to deduce possible dissociation scheme.

Many different (non-equivalent) slip planes can be considered for each of these slip plane because of the complex crystal structure (Fig. S1). For slip along [111], we have identified ones with the minimum overlapped atomic volume shown in Fig. 10(d) from each of possible three {110} and four {112} slip planes (Fig. S1), and the two-dimensional views of overlapped atomic volume on the relevant $(\bar{1}01)$ and $(\bar{1}\bar{1}2)$ planes are shown in Figs. 10(b) and (c), respectively. Figs. 10(b) and (c) indicate that the 1/2[111] dislocation may make colinear dissociation into three partial dislocations on the $(\bar{1}01)$ plane and into two partial dislocations on the $(\bar{1}\bar{1}2)$ plane, as clearly seen in the cross-sectional views of overlapped atomic volume along the slip direction of [111] (Fig. 10(d)). This is in contrast to

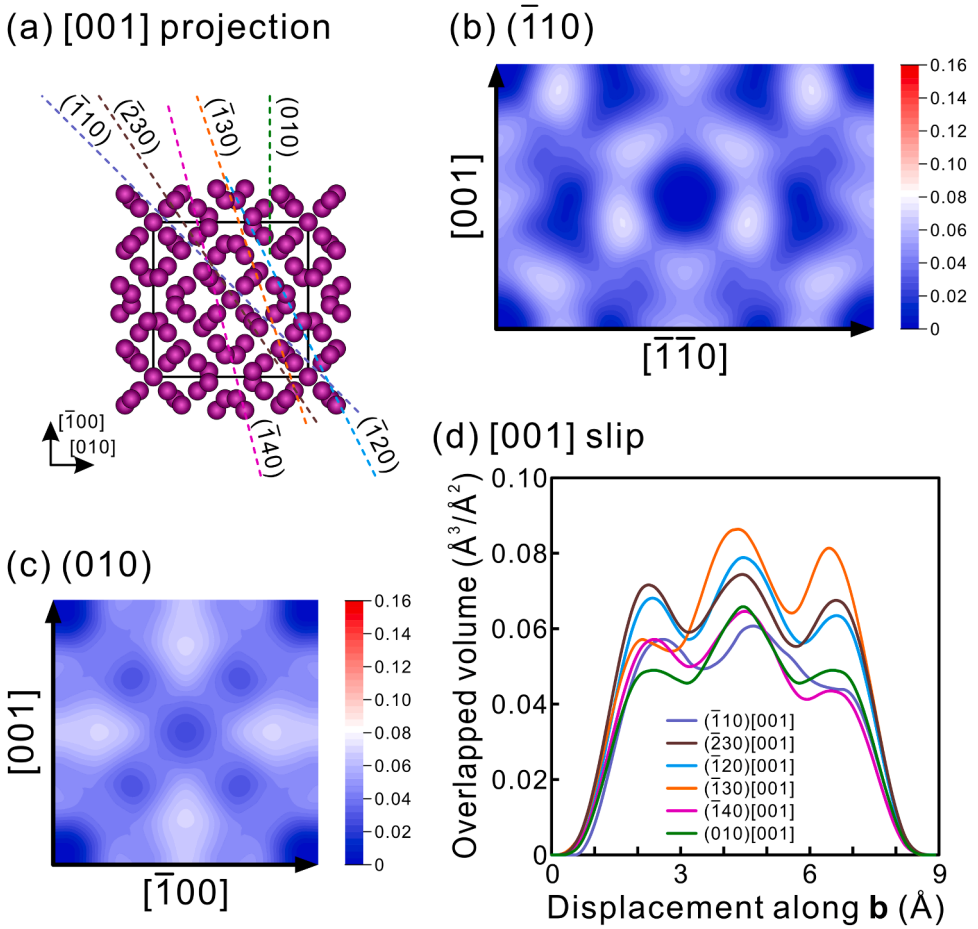

Fig. 11. (a) [001] projection of the crystal structure of α-manganese, showing the positions of $(\bar{1}10)$, $(\bar{2}30)$, $(\bar{1}20)$, $(\bar{1}30)$, $(\bar{1}40)$ and (010) slip planes with the minimum overlapped volume for shear along [001] among the relevant non-equivalent planes. Two-dimensional views of overlapped atomic volumes on (b) $(\bar{1}10)$ and (c) (010) slip planes indicated in (a). (d) Cross-sectional views of overlapped atomic volume along the slip direction of [001] on the $(\bar{1}10)$, $(\bar{2}30)$, $(\bar{1}20)$, $(\bar{1}30)$, $(\bar{1}40)$ and (010) slip planes.

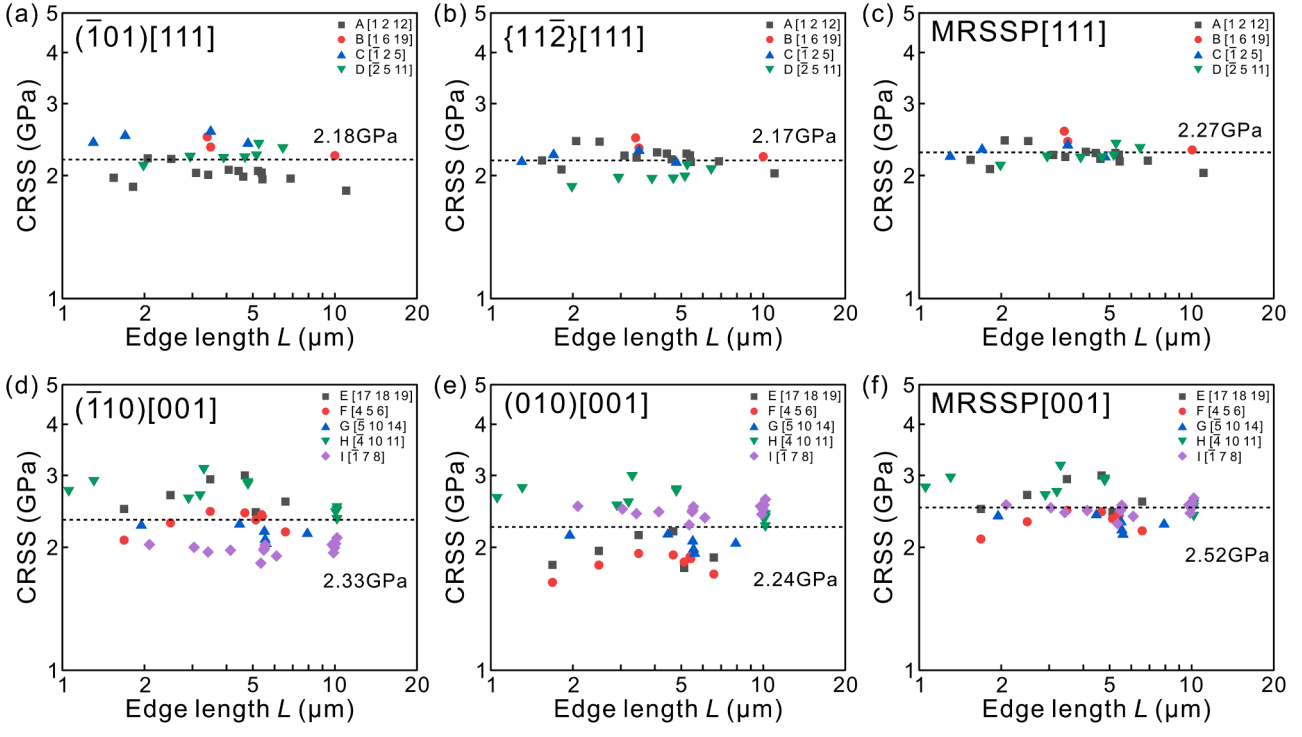

Fig. 12. Specimen-size dependence of CRSS for slip along [111] on (a) (1̄01), (b) {112} and (c) MRSSP and for slip along [001] on (d) (1̄10), (e) (010) and (f) MRSSP. The CRSS value calculated as the averaged value over the specimen size are indicated as a dotted line in each plot.

what is observed by experiment (Fig. 8). Fig. 10(d) indicates that for slip along [111], $(\bar{1}01)$ seems to be preferred to $(\bar{1}\bar{1}2)$ as the slip plane when judged the gradient of overlapped atomic volume. This is again in contrast to the result of slip trace analysis (Fig. 7(a)) that {112} rather than {110} is preferred as the slip plane. Fig. 10(d) also indicates the colinear three-fold dissociation of the 1/2[111] dislocation, which is also in contrast to what is observed by experiment (Fig. 5). The reason for the contradiction between the overlap volume calculation and experiment has yet to be clarified but may be found in the fact that the calculation was made without taking care of any thermal activation processes.

For slip along [001], slip tends to occur on the MRSSP, although slip lines are considerably wavy. This indicates either that cross-slip occurs frequently between some inherent low-indexed slip planes such as {010} and {110} or that cross-slip as well as slip occurs to include even some high-indexed slip planes such as {120} and {230}. As in the case of slip along [111], we have identified ones with the minimum overlapped atomic volume from each of possible slip planes including {100}, {110}, {120}, {130}, {140} and {230} (Fig. 11(a)). To note here is that the $(\bar{1}01)$ plane with the minimum overlapped volume for slip along [001] is calculated to be different from that for slip along [111]. The two-dimensional views of overlapped atomic volume on the relevant $(\bar{1}10)$ and (010) planes with the minimum overlap volume respectively shown in Figs. 11(b) and (c) indicate that the [010] dislocation may dissociate into three colinear partial dislocations. This is also observed in the cross-sectional views of overlapped atomic volume along the slip direction of [001] for all other slip planes (Fig. 11(d)). However, the stacking fault energies bounded by these partial dislocations seem to be high enough to avoid such dislocation dissociation on any possible slip planes. This is consistent with what is observed by experiment (Fig. 9). Fig. 11(d) also indicates that for slip along [001], it is practically impossible to select a particular slip plane from a several different possible slip planes, as their gradient of overlapped atomic volume are all similar to each other. This may be the reason why slip along [001] tends to occur on the MRSSP (Fig. 7(b)).

In α-manganese, while the slip direction (either [111] and [001]) is easily determined, their slip plane cannot uniquely be determined. This is similar to BCC metals, although the occurrence of slip along [001] has never been reported in BCC metals. The difficulty in the slip plane determination obviously comes from the wavy nature of slip line for both BCC metals and α-manganese, indicative of the occurrence of frequent cross slip. However, the dislocation structure in α-manganese indicates the absence of any preferred orientation for dislocation alignment, unlike in BCC metals in which 1/2<111> screw dislocations dominate in the deformation structure. The absence of any preferred orientation for dislocation alignment in α-manganese indicates the Peierls valley for dislocation motion is not particularly high along some particular orientations but is almost equally high for any directions. The occurrence of frequent cross-slip without any preferred orientation for dislocation alignment is similarly observed in aluminum, although the Peierls stress for dislocation motion is believed to be negligibly small in aluminum.

4.2. *Critical resolved shear stress and orientation-dependent operative slip systems*

As the slip planes (of low-index) for slip along [111] and [001] could not uniquely determined, some slip planes must be assumed to calculate the critical resolved shear stress (CRSS) values. We calculate the CRSS values assuming $(\bar{1}01)$ (Fig. 12(a)) and {112} (Fig. 12(b)) as the slip plane for slip along [111], and assuming $(\bar{1}10)$ (Fig. 12(d)) and (010) (Fig. 12(e)) as the slip plane for slip along [001]. We also calculate the CRSS values assuming the MRSSP as the slip plane for slip along [111] (Fig. 12(c)) and [001] (Fig. 12(f)). For all cases, the trend of CRSS to decrease with the increase in specimen size is not clear but it stays almost constant over a range of specimen size. The CRSS values are thus deduced as the average values, as indicated in each of figures of Fig. 12. The CRSS value (2.17∼2.27

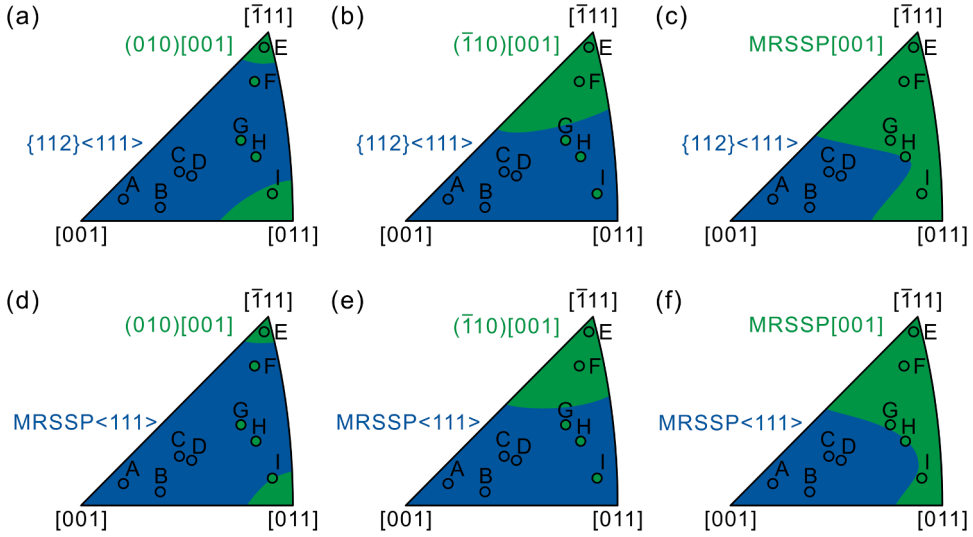

Fig. 13. The expected orientation-dependent operative slip systems under uniaxial loading calculated based on the CRSS values estimated in Fig. 12 for different combinations of slip planes for slip along ⟨111⟩ and [001].

GPa) for slip along [111] seems a bit lower than that (2.24∼2.52 GPa) for slip along [001]. The CRSS values for α-manganese are comparable to those for some brittle intermetallics such as σ-FeCr (1.33∼1.55 GPa (Kishida et al., 2022c) and are lower than those for some hard ceramics such as 6*H*-SiC (5∼10 GPa (Kishida et al., 2020d)). Such high CRSS values together with their negligibly small size dependence are considered to indicate that the CRSS values correspond to the stress required to introduce new dislocations from the edge or surface of micropillar specimens (Kishida et al., 2020c; 2020d). For slip along [001], while a large scatter in CRSS at a given specimen size is seen when $(\bar{1}10)$ and (010) are assumed to be the slip plane (Figs. 12(d) and (e)), such scatter is reduced considerably when the MRSSP is assumed (Fig. 12(f)). This may support the experimental finding of Fig. 7(b) that slip along [001] tends to occur on the MRSSP. For slip along [111], the reduction of scatter in CRSS occurs also when the MRSSP is assumed as the slip plane (Fig. 12(c)), although the extent of reduction is not as large as that in the case of slip along [001]. Of interest to notice in Fig. 12(b) is that there is no significant difference in CRSS for shear in the twinning sense (slip on $(\bar{2}11)$: orientation D) and for shear in the unti-twinning sense (slip on $(\bar{1}\bar{1}2)$: orientations A and B). This is different from what is usually observed for b.c.c. metals (Christian, 1983; Weinberger et al., 2013).

Fig. 13 illustrates the expected orientation-dependent operative slip systems under uniaxial loading calculated based on the CRSS values estimated in Fig. 12 for different combinations of slip planes for slip along ⟨111⟩ and [001]. We excluded the $\{\bar{1}01\}$ plane as the slip plane for slip along ⟨111⟩ as the ψ-χ plot of Fig. 7(a) clearly denies. The expected orientation ranges for slip along ⟨111⟩ and [001] are illustrated with different colors in the stereographic triangle together with the experimental results (orientations A-I). The slip plane for slip along ⟨111⟩ assumed is {112} (Figs. 13(a)-(c)) and MRSSP (Figs. 13(d)-(F)), and they are combined with (010) (Figs. 13 (a) and (d)), $(\bar{1}10)$ (Figs. 13(b) and (e)) and MRSSP (Figs. 13(c) and (F)) as the slip plane for slip along [001]. The expected orientation ranges for slip along ⟨111⟩ and [001] calculated with the CRSS values coincide with the experimental results only when {112}<111> and MRSSP[001] (Fig. 13(c)) and when MRSSP<111> and MRSSP[001] (Fig. 13(f)) are selected as the operative slip systems. This strongly indicates that while the slip plane can be {112} for slip along ⟨111⟩, slip along ⟨111⟩ and that along [001] both tend to occur on the MRSSP with frequent cross-slip among different slip planes.

The combination of the two different slip vectors (<111> and [001]) that are activated at comparable stress levels should offer a sufficient number of independent slip systems to ensure the general deformation of polycrystalline α-manganese. The occurrence of premature failure in α-manganese in the bulk form may then be ascribed mainly to the existence of flaws at grain boundary regions introduced during phase transformations upon cooling (Fig. 3(d,e)) and partly to the other factors such as inherent brittleness, stress concentrations resulting from elastic anisotropy and weakness of grain boundaries.

4.3. Comparison with $Mg_{17}Al_{12}$ (isostructural with α-manganese)

$Mg_{17}Al_{12}$, the strengthening phase of some diecast Mg alloy such as AZ63 and AZ91, is known to be isostructural with α-manganese. Because of its technological importance, the deformation behavior of $Mg_{17}Al_{12}$ has been investigated repeatedly (Hagihara et al., 2018; Mathur et al., 2016; Ragani et al., 2011; Xiao et al., 2013). Recently, Xiao et al. calculated generalized stacking fault energies (GSFEs) using density-functional theory (DFT) and made speculation of operative slip systems in $Mg_{17}Al_{12}$ (Xiao et al., 2013). The slip systems they considered are (100)[100], (110)[110], (110)[001] and {111}[112]. They concluded that (110)[110] slip is the most probable operative slip system. More recently, Hagihara and Hayakawa investigated the deformation behavior of single crystals of $Mg_{17}Al_{12}$ and found that {110}<111> slip is the only operative slip system activated above 300 °C (Hagihara et al., 2018), in contrast to the prediction by Xiao et al. (Xiao et al., 2013). Although Hagihara and Hayakawa described that slip lines for {110}<111> slip are wavy, they did not describe any deviation of these wavy slip line from the exact traces of {110} (Hagihara et al., 2018). Moreover, they did not observe slip along [001]. Their results are thus quite different from what is observed in α-manganese in the present study. The difference in chemical bonding (pure element (α-manganese) versus ordered intermetallic ($Mg_{17}Al_{12}$)) may account for the different operative slip systems in isostructural materials. Micropillar compression experiment on $Mg_{17}Al_{12}$ is currently in progress in our research group to clarify the origin of these differences.

5. Conclusions

Micropillar compression tests were carried out at room temperature on α-manganese single crystals as a function of the loading axis orientation and specimen size. The results obtained are summarized as follows.

1 α-manganese single crystals can plastically deform by dislocation motion at room temperature when the specimen size is reduced to the micrometer-range, accompanied by very high yield stresses of the range of 4–6 GPa.
2 Slip along [111] and [001] are identified to operate in compression-axis orientations near [001] and near [011] and $[\bar{1}11]$, respectively. Any low-indexed planes cannot be designated as the slip plane for both slip along [111] and [001], because of the significantly wavy nature of slip lines caused by the occurrence of frequent cross-slip.
3 The 1/2[111] dislocation carrying slip along [111] moves as a perfect dislocation without dissociation into partials and does not have any preferred orientation. The [001] dislocation carrying slip along [001] also moves as a perfect dislocation without dissociation into partials.

CRediT authorship contribution statement

Kyosuke Kishida: Investigation, Data curation, Visualization, Writing – original draft, Writing – review & editing, Funding acquisition. **Hirotaka Suzuki:** Investigation, Data curation, Visualization. **Masaomi Okutani:** Investigation, Data curation, Visualization. **Haruyuki Inui:** Supervision, Conceptualization, Methodology, Funding acquisition, Writing – original draft, Writing – review & editing.

Declaration of Competing Interest

The authors declare that they have no known competing financial interests or personal relationships that could have appeared to influence the work reported in this paper.

Acknowledgements

This work was supported by JSPS KAKENHI grant numbers JP18H05478, JP18H05450, JP18H05451, JP20K21084, JP21H01651, JP19H00824, JP19K22053 and the Elements Strategy Initiative for Structural Materials (ESISM) from the Ministry of Education, Culture, Sports, Science and Technology (MEXT) of Japan (Grant number JPMXP0112101000).

Supplementary materials

Supplementary material associated with this article can be found, in the online version, at doi:10.1016/j.ijplas.2022.103510.

References

ASM Int. Handbook Comm, 1990. Properties and Selection: irons, Steels, and High-Performance Alloys In: Metals Handbook, 10th ed., 1. ASM International, Ohio.

Chen, Z., Paul, B., Majumdar, S., Okamoto, N.L., Kishida, K., Inui, H., Otani, S., 2021. Room-temperature deformation of single crystals of ZrB_2 and TiB_2 with the hexagonal AlB_2 structure investigated by micropillar compression. Sci. Rep. 11, 14265. https://doi.org/10.1038/s41598-021-93693-9.

Christian, J.W., 1983. Some surprising features of the plastic deformation of body-centered cubic metals and alloys. Metall. Trans. A 14, 1237–1256. https://doi.org/10.1007/BF02664806.

Csanádi, T., Castle, E., Reece, M.J., Dusza, J., 2019. Strength enhancement and slip behavior of high-entropy carbide grains during micro-compression. Sci. Rep. 9, 10200. https://doi.org/10.1038/s41598-019-46614-w.

Cui, Y., Po, G., Srivastava, P., Jiang, K., Gupta, V., 2020. The role of slow screw dislocations in controlling fast strain avalanche dynamics in body-centered cubic metals. Int. J. Plast. 124, 117–132. https://doi.org/10.1016/j.ijplas.2019.08.008.

Dehm, G., Jaya, B.N., Raghavan, R., Kirchlechner, C., 2018. Overview on micro-and nanomechanical testing: new insights in interface plasticity and fracture at small length scales. Acta Mater. 142, 248–282. https://doi.org/10.1016/j.actamat.2017.06.019.

Dell, R.M., 2000. Batteries – fifty years of materials development. Solid State Ionics 134, 139–158. https://doi.org/10.1016/S0167-2738(00)00722-0.

Dunstan, D.J., Bushby, A.J., 2013. The scaling exponent in the size effect of small scale plastic deformation. Int. J. Plast. 40, 152–162. https://doi.org/10.1016/j.ijplas.2012.08.002.

Frank, F.C., Kasper, J.S., 1959. Complex alloy structures regarded as sphere packings. II. Analysis and classification of representative structures. Acta Cryst. 12, 483–499, 10.1107/S0365110x59001499.

Hagihara, K., Hayakawa, K., 2018. Plastic deformation behavior and operative slip systems in $Mg_{17}Al_{12}$ single crystals. Mater. Sci. Eng. A. 737, 393–400. https://doi.org/10.1016/j.msea.2018.09.056.

Hashizume, Y., Inomoto, M., Takebayashi, H., Okamoto, N.L., Inui, H., 2020. Micropillar compression deformation of single crystals of the intermetallic compound Γ-Fe_4Zn_9. Acta Mater. 199, 514–522. https://doi.org/10.1016/j.actamat.2020.08.062.

Hashizume, Y., Inomoto, M., Okamoto, N.L., Inui, H., 2021. Plastic deformation of single crystals of the δ_{1p} and δ_{1k} intermetallic compounds in the Fe-Zn system by micropillar compression. Int. J. Plast. 136, 102889 https://doi.org/10.1016/j.ijplas.2020.102889.

Higashi, M., Momono, S., Kishida, K., Okamoto, N.L., Inui, H., 2018. Anisotropic plastic deformation of single crystals of the MAX phase compound Ti_3SiC_2 investigated by micropillar compression. Acta Mater. 161, 161–170. https://doi.org/10.1016/j.actamat.2018.09.024.

Inui, H., Okamoto, N.L., Yamaguchi, S., 2018. Crystal structures and mechanical properties of Fe-Zn intermetallic compounds formed in the coating layer of galvannealed steels. ISIS Int. 58, 1550–1561. https://doi.org/10.2355/isijinternational.ISIJINT-2018-066.

Kaufman, J.G., 2000. Introduction to Aluminum Alloys and Tempers. ASM International, Ohio.

Kishida, K., Chen, Z., Matsunoshita, H., Maruyama, T., Fukuyama, T., Sasai, Y., Inui, H., Heilmaier, M., 2020a. Plastic deformation of bulk and micropillar single crystals of Mo_5Si_3 with the tetragonal $D8_m$ structure. Int. J. Plast. 155, 103339 https://doi.org/10.1016/j.ijplas.2022.103339.

Kishida, K., Fukuyama, T., Maruyama, T., Inui, H., 2020b. Room temperature deformation of single crystals of Ti_5Si_3 with the hexagonal $D8_8$ structure investigated by micropillar compression tests. Sci. Rep. 10, 17983. https://doi.org/10.1038/s41598-020-75007-7.

Kishida, K., Maruyama, T., Fukuyama, T., Inui, H., 2020c. Micropillar compression deformation of single crystals of α-Nb_5Si_3 with the tetragonal $D8_l$ structure. Sci. Tech. Adv. Mater. 21, 805–816. https://doi.org/10.1080/14686996.2020.1855065.

Kishida, K., Maruyama, T., Matsunoshita, H., Fukuyama, T., Inui, H., 2018. Micropillar compression deformation of single crystals of Mo_5SiB_2 with the tetragonal $D8_l$ structure. Acta Mater. 159, 416–428. https://doi.org/10.1016/j.actamat.2018.08.048.

Kishida, K., Nakatsuka, S., Nose, H., Inui, H., 2022a. Room-temperature deformation of single crystals of transiton-metal disilicides ($TMSi_2$) with the $C11_b$ (TM = Mo) and C40 (TM = V, Cr, Nb and Ta) structures investigated by micropillar compression. Acta Mater. 223, 117468 https://doi.org/10.1016/j.actamat.2021.117468.

Kishida, K., Okutani, M., Inui, H., 2022b. Direct observation of zonal dislocation in complex materials by atomic-resolution scanning electron microscopy. Acta Mater. 228, 117756 https://doi.org/10.1016/j.actamat.2022.117756.

Kishida, K., Okutani, M., Suzuki, H., Inui, H., Heilmaier, M., Raabe, D., 2022c. Room-temperature deformation of single crystals of the sigma-phase compound FeCr with the tetragonal $D8_b$ structure investigated by micropillar compression. Acta Mater. Submitted.

Kishida, K., Shinkai, Y., Inui, H., 2020d. Room temperature deformation of 6*H*-SiC single crystals investigated by micropillar compression. Acta Mater. 187, 19–28. https://doi.org/10.1016/j.actamat.2020.01.027.

Korte, S., Clegg, W.J., 2011. Discussion of the dependence of the effect of size on the yield stress in hard materials studied by microcompression of MgO. Philos. Mag. 91, 1150–1162. https://doi.org/10.1080/14786435.2010.505179.

Korte-Kerzel, S., 2017. Microcompression of brittle and anisotropic crystals: recent advances and current challenges in studying plasticity in hard materials. MRS Comm. 7, 109–120. https://doi.org/10.1557/mrc.2017.15.
Kratochvíl, J., Málek, J., Minakowski, P., 2016. A Gibbs-potential-based framework for ideal plasticity of crystalline solids treated as a material flow through an adjustable crystal lattice space and its application to three-dimensional micropillar compression. Int. J. Plast. 87, 114–129. https://doi.org/10.1016/j.ijplas.2016.09.006.
Lin, P., Liu, Z., Zhuang, Z., 2016. Numerical study of the size-dependent deformation morphology in micropillar compressions by a dislocation-based crystal plasticity model. Int. J. Plast. 87, 32–47. https://doi.org/10.1016/j.ijplas.2016.09.001.
Mapar, A., Ghassemi-Armaki, H., Pourboghrat, F., Kumar, K.S., 2017. A differential-exponential hardening law for non-Schmid crystal plasticity finite element modeling of ferrite single crystals. Int. J. Plast. 91, 268–299. https://doi.org/10.1016/j.ijplas.2016.11.009.
Martha, S.K., Markovsky, B., Grinblat, J., Gofer, Y., Haik, O., Zinigrad, E., Aurbach, D., Drezen, T., Wang, D., Deghenghi, G., Exnar, I., 2009. LiMnPO4 as an advanced cathode material for rechargeable lithium batteries. J. Electrochem. Soc. 156, A541–A552. https://doi.org/10.1149/1.3125765.
Mathur, H.N., Maier-Kiener, V., Korte-Kerzel, S., 2016. Deformation in the γ-$Mg_{17}Al_{12}$ phase at 25-278 °C. Acta Mater. 113, 221–229. https://doi.org/10.1016/j.actamat.2016.05.001.
Matricardi, L.R., Downing, J., 2000. Manganese and Manganese Alloys, in: Kirk, R.E., Othmer, D.F. (Eds.), Kirk-Othmer Encyclopedia of Chemical Technology, 5th ed., Vol.15, Wiley, Hoboken, pp.538–565.10.1002/0471238961.1301140713012018.a01.pub3.
Meaden, G.T., 1968. The general physical properties of manganese metal. Metall. Reviews. 13, 97–114. https://doi.org/10.1179/mtlr.1968.13.1.97.
Michler, J., Wasmer, K., Meier, S., Östlund, F., Leifer, K., 2007. Plastic deformation of gallium arsenide micropillars under uniaxial compression at room temperature. Appl. Phys. Lett. 90, 043123 https://doi.org/10.1063/1.2432277.
Okamoto, N.L., Inomoto, M., Adachi, H., Takebayashi, H., Inui, H., 2014. Micropillar compression deformation of single crystals of the intermetallic compound ζ-$FeZn_{13}$. Acta Mater. 65, 229–239. https://doi.org/10.1016/j.actamat.2013.10.065.
Okamoto, N.L., Kashioka, D., Inomoto, M., Inui, H., Takebayashi, H., Yamaguchi, S., 2013. Compression deformability of Γ and ζ Fe-Zn intermetallics to mitigate detachment of brittle intermetallic coating of galvannealed steels. Scripta Mater 69, 307–310. https://doi.org/10.1016/j.scriptamat.2013.05.003.
Proult, A., Donnadieu, P., 1995. A simple description of the α-manganese (A12) structure derived from defect studies. Philos. Mag. Lett. 72, 337–344. https://doi.org/10.1080/09500839508242472.
Ragani, J., Donnadieu, P., Tassin, C., Blandin, J.J., 2011. High-temperature deformation of the γ-$Mg_{17}Al_{12}$ complex metallic alloy. Scripta Mater. 65, 253–256. https://doi.org/10.1016/j.scriptamat.2011.04.022.
Schröders, S., Sandlöbes, S., Birke, C., Loeck, M., Peters, L., Tromas, C., Korte-Kerzel, S., 2018. Room temperature deformation in Fe_7Mo_6 μ-phase. Int. J. Plast. 108, 125–143. https://doi.org/10.1016/j.ijplas.2018.05.002.
Sully, A.H., 1955. Manganese (Metallurgy of the Rarer Metals –3). Butterworth, London.
Takata, N., Ghassemi Armaki, H., Terada, Y., Takeyama, M., Kumar, K.S., 2013. Plastic deformation of the C14 Laves phase $(Fe,Ni)_2Nb$. Scripta Mater. 68, 615–618. https://doi.org/10.1016/j.scriptamat.2012.12.019.
Uchic, M.D., Shade, P.A., Dimiduk, D.M., 2009. Plasticity of micrometer-scale single crystals in compression. Annu. Rev. Mater. Res. 39, 161–186. https://doi.org/10.1146/annurev-matsci-082908-145422.
Watson, R.E., Bennett, L.H., 1985. Alpha manganese and the Frank Kasper phases. Scripta Metall. 19, 535–538. https://doi.org/10.1016/0036-9748(85)90129-2.
Weaver, J.S., Li, N., Mara, N.A., Jones, D.R., Cho, H., Bronkhorst, C.A., Fensin, S.J., Gray, G.T., 2018. Slip transmission of high angle grain boundaries in body-centered cubic metals: micropillar compression of pure Ta single and bi-crystals. Acta Mater. 156, 356–368. https://doi.org/10.1016/j.actamat.2018.06.046.
Weinberger, C.R., Boyce, B.L., Battaile, C.C., 2013. Slip planes in bcc transition metals. Int. Mater. Rev. 58, 296–314. https://doi.org/10.1179/1743280412Y.0000000015.
Xiao, W., Zhang, X., Geng, W.T., Lu, G., 2013. Atomistic study of plastic deformation in Mg-Al alloys. Mater. Sci. Eng. A. 586, 245–252. https://doi.org/10.1016/j.msea.2013.07.093.
Zhang, J., Kishida, K., Inui, H., 2017. Specimen size and shape dependent yield strength in micropillar compression deformation of Mo single crystals. Int. J. Plast. 92, 45–56. https://doi.org/10.1016/j.ijplas.2017.02.014.
Zhang, J.Y., Liu, G., Sun, J., 2013. Strain rate effects on the mechanical response in multi- and single crystalline Cu micropillars: grain boundary effects. Int. J. Plast. 50, 1–17. https://doi.org/10.1016/j.ijplas.2013.03.009.
Zhao, X.X., Wu, J., Chiu, Y.L., Jones, I.P., Gu, R., Ngan, A.H.W., 2019. Critical dimension for the dislocation structure in deformed copper micropillars. Scripta Mater. 163, 137–141. https://doi.org/10.1016/j.scriptamat.2019.01.020.